1 **Assessing the simulated soil thermal regime from Noah-MP LSM**

2 **v1.1 for near-surface permafrost modeling on the Qinghai-Tibet**

3 **Plateau**

4

5 Xiangfei Li[1,2], Tonghua Wu[1,*], Xiaodong Wu[1], Xiaofan Zhu[1], Guojie Hu[1], Ren Li[1],

6 Yongping Qiao[1], Cheng Yang[1,2], Junming Hao[1,2], Jie Ni[1,2], Wensi Ma[1,2]

7

8 [1] Cryosphere Research Station on the Qinghai-Tibet Plateau, State Key Laboratory of

9 Cryospheric Science, Northwest Institute of Eco-Environment and Resources, Chinese

10 Academy of Sciences, Lanzhou 730000, China

11 [2] University of Chinese Academy of Sciences, Beijing 100049, China

12

13 **Correspondence:** Tonghua Wu (thuawu@lzb.ac.cn)

14

15   **Abstract.** Land surface models (LSMs) are effective tools for near-surface permafrost

16   modeling. Extensive and rigorous model inter-comparison is of great importance before

17   application due to the uncertainties in current LSMs. This study designed an ensemble

18   of 6912 experiments to evaluate the Noah land surface model with multi-

19   parameterization (Noah-MP) for soil temperature (ST) simulation, and investigate the

20   sensitivity of parameterization schemes at a typical permafrost site on the Qinghai-Tibet

21   Plateau. The results showed that Noah-MP generally underestimates ST, especially that

22   during the cold season. In addition, the simulation uncertainty is greater in the cold

23   season (October-April) and for the deep soil layers. ST is most sensitive to surface layer

24   drag coefficient (SFC) while largely influenced by runoff and groundwater (RUN). By

25   contrast, the influence of canopy stomatal resistance (CRS) and soil moisture factor for

26   stomatal resistance (BTR) on ST is negligible. With limited impacts on ST simulation,

27   vegetation model (VEG), canopy gap for radiation transfer (RAD) and snow/soil

28   temperature time scheme (STC) are more influential on shallow ST, while super-cooled

29   liquid water (FRZ), frozen soil permeability (INF) and lower boundary of soil

30   temperature (TBOT) have greater impacts on deep ST. Furthermore, an optimal

31   configuration of Noah-MP for permafrost modeling were extracted based on the

32   connectivity between schemes, and they are: table leaf area index with calculated

33   vegetation fraction, Jarvis scheme for CRS, Noah scheme for BTR, BATS model for

34   RUN, Chen97 for SFC, zero canopy gap for RAD, variant freezing-point depression

35   for FRZ, hydraulic parameters defined by soil moisture for INF, ST at 8 m for TBOT,

36   and semi-implicit method for STC. The analysis of the model structural uncertainties

37   and characteristics of each scheme would be constructive to a better understanding of

38   the land surface processes on the QTP and further model improvements towards near-

39   surface permafrost modeling using the LSMs.

40

1 Introduction

The Qinghai-Tibet Plateau (QTP) hosts the world's largest high-altitude permafrost covering a contemporary area of 1.06×10^6 km^2 (Zou et al., 2017). Under the background of climate warming and intensifying human activities, permafrost on the QTP has been widely suffering thermal degradation (Ran et al., 2018), resulting in reduction of permafrost extent, disappearing of permafrost patches and thickening of active layer (Chen et al., 2020). Moreover, such degradation could cause alterations in hydrological cycles (Zhao et al., 2019; Woo, 2012), changes on ecosystem (Fountain et al., 2012; Yi et al., 2011) and damages to infrastructures (Hjort et al., 2018). Therefore, it is very important to monitor and simulate the state of permafrost to adapt to the degradation.

Soil temperature (ST) is an intuitive indicator to evaluate the thermal state of permafrost. A number of monitoring sites have been established on the QTP (Cao et al., 2019). However, it is inadequate to construct the thermal state of permafrost by considering the spatial variability of the ground thermal regime and an uneven distribution of these observations. In contrast, numerical models are competent alternatives. In recent years, land surface models (LSMs), which describe the exchanges of heat, water, and momentum between the land and atmosphere (Maheu et al., 2018), have received significant improvements in the representation of permafrost and frozen ground processes (Koven et al., 2013; Nicolsky et al., 2007; Melton et al., 2019). LSMs are capable of simulating the transient change of permafrost by describing subsurface hydrothermal processes (e.g. soil temperature and moisture) with soil heat conduction (-diffusion) and water movement equations (Daniel et al., 2008). Moreover, they can be integrated with the numerical weather prediction system like WRF (Weather Research and Forecasting), making them as effective tools for comprehensive interactions between climate and permafrost (Nicolsky et al., 2007).

Some LSMs have been applied to modeling permafrost in the QTP. Guo and Wang (2013) investigated near-surface permafrost and seasonally frozen ground states as well as their changes using the Community Land Model, version 4 (CLM4). Hu et al. (2015)

70   applied the coupled heat and mass transfer model to identify the hydrothermal

71   characteristics of the permafrost active layer in the Qinghai-Tibet Plateau. Using an

72   augmented Noah LSM, Wu et al. (2018) modeled the extent of permafrost, active layer

73   thickness, mean annual ground temperature, depth of zero annual amplitude and ground

74   ice content on the QTP in 2010s. Despite those achievements based on different models,

75   LSMs are in many aspects insufficient for permafrost modeling. For one thing, large

76   uncertainties still exist in the state-of-the-art LSMs when simulating the soil

77   hydrothermal regime on the QTP (Chen et al., 2019). For instance, 19 LSMs in CMIP5

78   overestimate snow depth over the QTP (Wei and Dong, 2015), which could result in the

79   variations of the soil thermal regime in the aspects of magnitude and vector (cooling or

80   warming) (Zhang, 2005). Moreover, most of the existing LSMs are not originally

81   developed for permafrost modeling. Many of their soil processes are designed for

82   shallow soil layers (Westermann et al., 2016), but permafrost may occur in the deep

83   soil. And the soil column is often considered homogeneous, which can not represent

84   the stratified soil common on the QTP (Yang et al., 2005). Given the numerous LSMs

85   and possible deficiencies, it is necessary to assess the parameterization schemes for

86   permafrost modeling on the QTP, which is helpful to identify the influential sub-

87   processes, enhance our understanding of model behavior, and guide the improvement

88   of model physics (Zhang et al., 2016).

89   Noah land surface model with multi-parameterization (Noah-MP) provides a

90   unified framework in which a given physical process can be interpreted using multiple

91   optional parameterization schemes (Niu et al., 2011). Due to the simplicity in selecting

92   alternative schemes within one modeling framework, it has been attracting increasing

93   attention in inter-comparison work among multiple parameterizations at point and

94   watershed scales (Hong et al., 2014; Zheng et al., 2017; Gan et al., 2019; Zheng et al.,

95   2019; Chang et al., 2020; You et al., 2020). For example, Gan et al. (2019) carried an

96   ensemble of 288 simulations from multi-parameterization schemes of six physical

97   processes, assessed the uncertainties of parameterizations in Noah-MP, and further

98   revealed the best-performing schemes for latent heat, sensible heat and terrestrial water

99   storage simulation over ten watersheds in China. You et al. (2020) assessed the

100 performance of Noah-MP in simulating snow process at eight sites over distinct snow

101 climates and identified the shared and specific sensitive parameterizations at all sites,

102 finding that sensitive parameterizations contribute most of the uncertainties in the

103 multi-parameterization ensemble simulations. Nevertheless, there is little research on

104 the inter-comparison of soil thermal processes toward permafrost modeling. In this

105 study, an ensemble experiment of totally 6912 scheme combinations was conducted at

106 a typical permafrost monitoring site on the QTP. The simulated soil temperature (ST)

107 of Noah-MP model was assessed and the sensitivities of parameterization schemes at

108 different depth were further investigated. Considering the general performance and

109 sensitive schemes of Noah-MP, we further explored the interactions between the most

110 influential schemes and configured an optimal combination based on the connections

111 between schemes. We hope this study can provide a reference for permafrost simulation

112 on the QTP.

113   This article is structured as follows: Section 2 introduces the study site,

114 atmospheric forcing data, design of ensemble simulation experiments, and sensitivity

115 analysis and optimal selection methods. Section 3 describes the ensemble simulation

116 results of ST, explores the sensitivity and interactions of parameterization schemes, and

117 determines the optimal combination for permafrost modeling. Section 4 discusses the

118 schemes in each physical process and proposes further research topics. Section 5

119 concludes the main findings of this study.

120 **2   Methods and materials**

121 **2.1 Site description and observation datasets**

122   Tanggula observation station (TGL) lies in the continuous permafrost regions of

123 Tanggula Mountain, central QTP (33.07°N, 91.93°E, Alt.: 5,100 m a.s.l; Fig. 1). This

124 site is characterized by the sub-frigid and semiarid climate (Li et al., 2019). According

125 to the observations from 2010−2011, the annual mean air temperature of TGL site was

126 −4.4 °C. The annual precipitation was 375 mm, and of which 80% is concentrated

127 between May and September. Alpine steppe with low height is the main land surface,

128 whose coverage range is about 40% ~ 50% (Yao et al., 2011). The active layer thickness

129 is about 3.15 m (Hu et al., 2017).

130 　　The atmospheric forcing data, including wind speed/direction, air

131 temperature/relative humidity/pressure, downward shortwave/longwave radiation, and

132 precipitation, were used to drive the model. These variables above were measured at a

133 height of 2 m and covered the period from August 10, 2010 to August 10, 2012 (Beijing

134 time) with a temporal resolution of 1 hour. Daily soil temperature from October 1, 2010

135 to September 30, 2011 (Beijing time) were utilized to validate the simulation results.
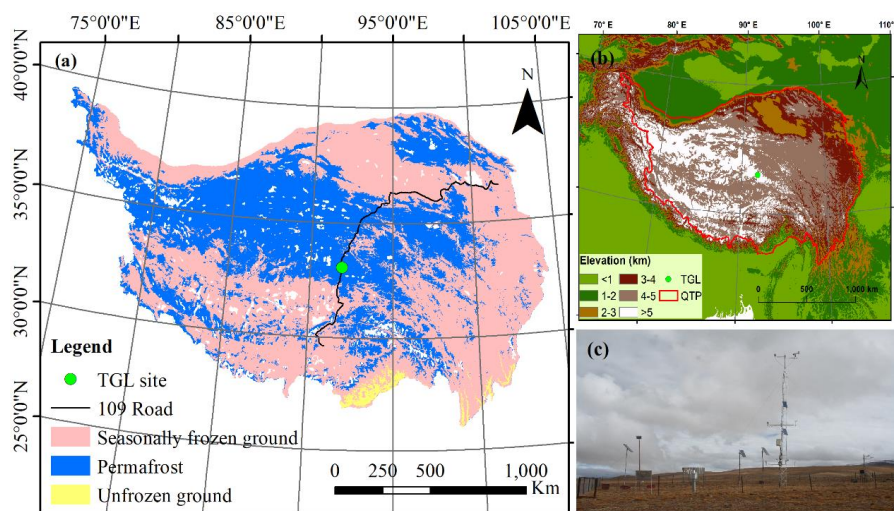
136

137 **Figure 1.** Location and geographic features of study site. (a) Location of observation

138 site and permafrost distribution (Zou et al., 2017). (b) Topography of the Qinghai-Tibet

139 Plateau. (c) Photo of the Tanggula observation station.

140 **2.2 Ensemble experiments of Noah-MP**

141 　　The offline Noah-MP LSM v1.1 was assessed in this study. It consists of 12

142 physical processes that are interpreted by multiple optional parameterization schemes.

143 These sub-processes include vegetation model (VEG), canopy stomatal resistance

144 (CRS), soil moisture factor for stomatal resistance (BTR), runoff and groundwater

145 (RUN), surface layer drag coefficient (SFC), super-cooled liquid water (FRZ), frozen

146 soil permeability (INF), canopy gap for radiation transfer (RAD), snow surface albedo

147 (ALB), precipitation partition (SNF), lower boundary of soil temperature (TBOT) and

148 snow/soil temperature time scheme (STC) (Table 1). Details about the processes and

149 optional parameterizations can be found in Yang et al. (2011a).

150   In this study, the dynamic vegetation option in VEG process was turned off for

151 simplicity. Previous studies has confirmed that Noah-MP seriously overestimate the

152 snow depth on the QTP (Li et al., 2020 (under review); Wang et al., 2020). However,

153 the impact of snow cover on ground temperatures in the permafrost regions of QTP is

154 usually considered weak (Jin et al., 2008; Wu et al., 2018), because the snow cover is

155 thin, short-lived, and patchy-distributed (Che et al., 2019). To avoid the possible bias

156 caused by snow process, the ALB and SNF processes were not considered. As a result,

157 in total 6912 combinations are possible for the left 10 processes and orthogonal

158 experiments were carried out to evaluate their performance in soil thermal dynamics

159 and obtain the optimal combination.

160   The monthly leaf area index (LAI) was derived from the Advanced Very High-

161 Resolution Radiometer (AVHRR) (https://www.ncei.noaa.gov/data/, Claverie et al.,

162 2016). The Noah-MP model was modified to consider the vertical heterogeneity in the

163 soil profile by setting the corresponding soil parameters for each layer. The soil

164 hydraulic parameters, including the porosity, saturated hydraulic conductivity,

165 hydraulic potential, the Clapp-Hornberger parameter b, field capacity, wilt point, and

166 saturated soil water diffusivity, were determined using the pedotransfer functions

167 proposed by Hillel (1980), Cosby et al. (1984), and Wetzel and Chang (1987), in which

168 the sand and clay percentages were based on Hu et al., (2017). In addition, the

169 simulation depth was extended to 8.0 m to cover the active layer thickness of the QTP.

170 The soil column was discretized following the default scheme in CLM 5.0 (Lawrence

171 et al., 2018). A 30-year spin-up was conducted in every simulation to reach equilibrium

172 soil states.

Table 1. The physical processes and options of Noah-MP. Options in bold are the

optimal selections in this study.

Physical processes	Options
Vegetation model (VEG)	(1) table LAI, prescribed vegetation fraction
	(2) dynamic vegetation
	(3) table LAI, calculated vegetation fraction
	(4) table LAI, prescribed max vegetation fraction
Canopy stomatal resistance (CRS)	**(1) Jarvis**
	(2) Ball-Berry
Soil moisture factor for stomatal resistance (BTR)	**(1) Noah**
	(2) CLM
	(3) SSiB
Runoff and groundwater (RUN)	(1) SIMGM with groundwater
	(2) SIMTOP with equilibrium water table
	(3) Noah (free drainage)
	(4) BATS (free drainage)
Surface layer drag coefficient (SFC)	(1) Monin-Obukhov (M-O)
	(2) Chen97
Super-cooled liquid water (FRZ)	(1) generalized freezing-point depression
	(2) Variant freezing-point depression
Frozen soil permeability (INF)	**(1) Defined by soil moisture, more permeable**
	(2) Defined by liquid water, less permeable
Canopy gap for radiation transfer (RAD)	(1) Gap=F(3D structure, solar zenith angle)
	(2) Gap=zero
	(3) Gap=1-vegetated fraction
Snow surface albedo (ALB)	(1) BATS
	(2) CLASS
Precipitation partition (SNF)	(1) Jordan91
	(2) BATS: $T_{sfc} < T_{frz}+2.2K$
	(3) $T_{sfc} < T_{frz}$
Lower boundary of soil temperature (TBOT)	1) zero heat flux
	2) soil temperature at 8m depth
Snow/soil temperature time scheme (STC)	**(1) semi-implicit**
	(2) full implicit

BATS (Biosphere–Atmosphere Transfer Model); CLASS (Canadian Land Surface Scheme);

SIMGM (Simple topography-based runoff and Groundwater Model); SIMTOP (Simple

Topography-based hydrological model); SSiB (Simplified Simple Biosphere model).

2.3 Methods for sensitivity analysis

The root mean square error (RMSE) and standard deviation (SD) between the

180   simulations and observations were adopted to evaluate the performance of Noah-MP.

181   The averages of the RMSEs and SDs of all the soil layers were defined as column

182   RMSE (colRMSE) and column SD (colRMSE), respectively.

183   To investigate the influence degrees of each physical process on ST, we firstly

184   calculated the mean RMSE ($\bar{Y}_j^i$) of the jth parameterization schemes ($j = 1, 2, …$) in the

185   ith process ($i = 1, 2, …$). Then, the maximum difference of $\bar{Y}_j^i$ ($\Delta\overline{RMSE}$) was defined

186   to quantify the sensitivity of the ith process ($i = 1, 2, …$):

$$\Delta\overline{RMSE} = \bar{Y}_{max}^i - \bar{Y}_{min}^i$$

188   where $\bar{Y}_{max}^i$ and $\bar{Y}_{min}^i$ are the largest and the smallest $\bar{Y}_j^i$ in the ith process,

189   respectively. For a given physical process, a high S_i signifies large difference between

190   parameterizations, indicating high sensitiveness of the ith process.

191   The sensitivities of physical processes were determined by quantifying the

192   statistical distinction level of performance between parameterization schemes. The

193   Independent-sample T-test (2-tailed) was adopted to identify whether the distinction

194   level between two schemes is significant, and that between three or more schemes was

195   tested using the Tukey's test. Tukey's test has been widely used for its simple

196   computation and statistical features (Benjamini, 2010). The detailed descriptions about

197   this method can be found in Zhang et al. (2016), Gan et al. (2019), and You et al. (2020).

198   A process can be considered sensitive when the schemes show significant difference.

199   Moreover, schemes with small mean RMSE were considered favorable for ST

200   simulation. We distinguished the differences of the parameterization schemes at 95%

201   confidence level.

202   **2.4 Optimal selection methods**

203   To extract the optimal combinations of parameterization schemes, the connection

204   frequency (CF) between parameterizations was calculated:

205   (1) Sorting the 6912 colRMSEs in an ascending order;

206   (2) Donating the colRMSEs concentrated below the 5th percentile as the "best

Geoscientific
Model Development
Discussions

207 combinations" (346 members);

208 (3) Counting the times of a given parameterizations occurring with other

209 parameterizations in the "best combinations";

210 (4) The CF was then determined by dividing 346.

211 Obviously, for two given parameterization schemes, a large CF has an advantage

212 in terms of optimal combination.

213 **3   Results**

214 **3.1 General performance of the ensemble simulation**

215 We evaluated ST from the 6912 experiments against observations. Figure. 2

216 illustrates the ensemble simulated and observed annual cycle of ST at TGL site. The

217 plots give the uncertainty ranges of the ensemble experiments using five statistical

218 indicators, i.e., the first/third quartile (Q1/Q3), mean, the lower (Q1-1.5(Q3-Q1)) and

219 upper bound (Q3+1.5(Q3-Q1)). The kernel density distribution of the simulated ST is

220 also illustrated. The ensemble experiments basically captured the seasonal variability

221 of ST, whose magnitude decreased with soil depth. In addition, the simulated ST in the

222 cold season (October-April) showed relatively wide uncertainty ranges, particularly at

223 the deep layers. This indicates that the selected schemes perform more differently

224 during the cold season, which is especially so at the deep layers. The simulated ST were

225 generally smaller than the observations with relatively large gap during the cold season.

226 It indicates that the Noah-MP model generally underestimates the ST, especially during

227 the cold season. Moreover, the simulated ST was widely found to be bimodal

228 distribution across the soil column, implying that two schemes dominate the ST

229 simulation in the Noah-MP model.
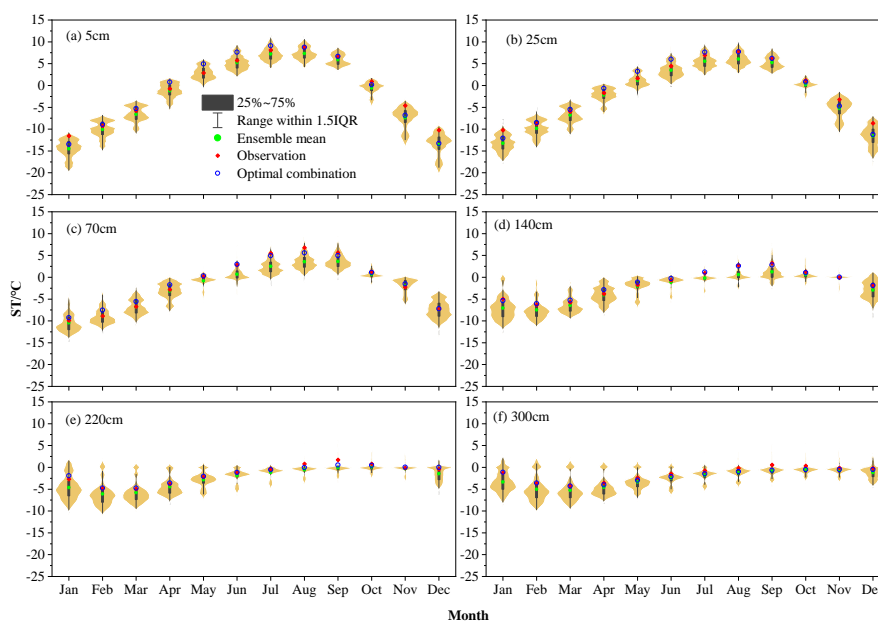
Figure 2. Monthly soil temperature (ST) at (a) 5 cm, (b) 25 cm, (c) 70 cm, (d) 140 cm, (e) 220 cm, (f) 300 cm at TGL site. Limits of the boxes represent upper and lower quartiles, whiskers extend to 1.5 times the interquartile range (IQR). The green circles in the box are the ensemble mean values. The light orange shading represents the kernel density distribution of simulated ST. The red diamonds are observations and the blue circles are the results of the optimal scheme combination.

3.2 Sensitivity of physical processes

3.2.1 Influence degrees of physical processes
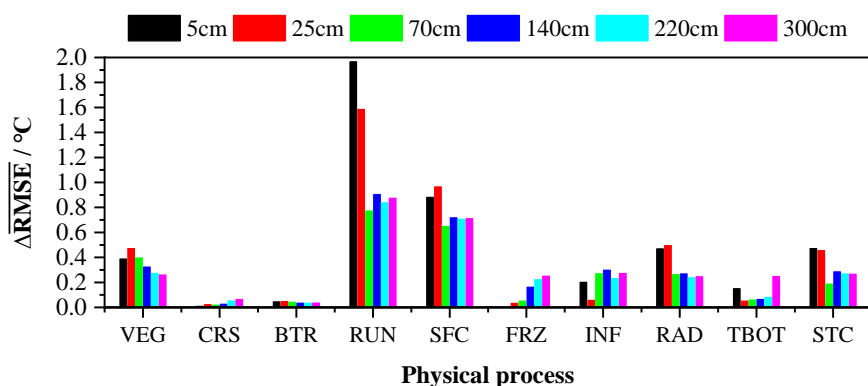
Figure 3. The maximum difference of the mean RMSE ($\Delta\overline{RMSE}$) in each physical process at different soil depths.

Figure. 3 compares the influence scores of the 10 physical processes at different soil depths, based on the maximum difference of the mean RMSE over 6912 experiments using the same scheme, for ST at TGL site. The RUN and SFC processes dominated the $\Delta\overline{RMSE}$ at all layers, indicating that they are the most sensitive processes for ST simulation. While the $\Delta\overline{RMSE}$ of the other 8 physical processes were all less than 0.5℃, among which the influence of CRS and BTR processes were negligible. What's more, the VEG, RAD and STC processes were more influential on the shallow STs than the deep STs. Taking the STC process as an example, the $\Delta\overline{RMSE}$ of the 5cm and 25 cm were nearly 0.5℃ while that of the 70 cm, 140cm, 220cm and 300cm were no more than 0.3℃. In contrast, the influence of FRZ, INF and TBOT processes were generally greater in deep soils than shallow soils.

Interactions between two of the most influential physical processes are analyzed in this section. The performance of the simulations with SFC and RUN were rated by rounding the colRMSEs and colSDs (Fig. 4). Given the colRMSE=1.2 for one simulation, then the score of the simulation equals 1 (SCORE=1) for the corresponding combination. It can be seen that SFC(1) in the SFC process and RUN(3) in the RUN

258 process were the major schemes that contribute to the cold bias of the ensemble

259 simulation, because they dominated the cold bias of the ensemble simulation with

260 relatively low colSD scores (Fig. 4b). Consistent with the bimodal distribution in Fig.

261 2, most of the simulations with relative low colRMSE and nearly zero colSD were

262 related to SFC(2). It indicates that combinations with SFC(2) result in better

263 performance than SFC(1) by improving the underestimations of ST. Among the

264 schemes in RUN, RUN(1), RUN(2) and RUN(4) had approximately equal chance to

265 produce better and worse performance for ST simulation, implying a dominating role

266 of the SFC process (Fig. 4a). RUN(3) produced much worse performance by

267 aggravating the underestimation of ST. Ultimately, the best results came from the

268 combination of SFC(2) and RUN(4), while the worst results were from the combination

269 of SFC(1) and RUN(3).
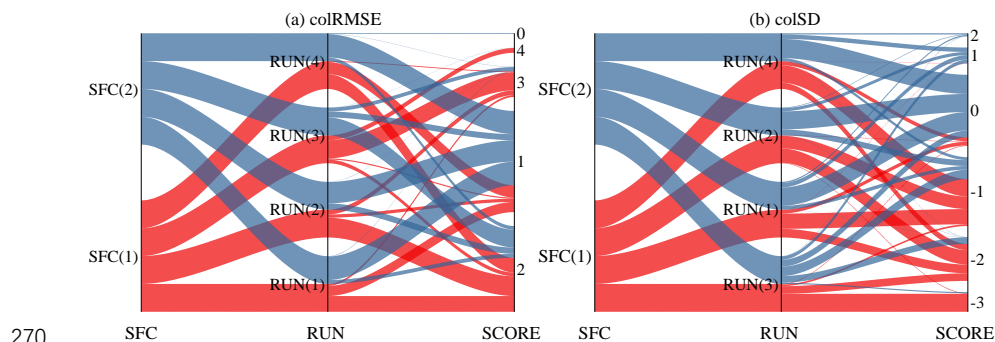
270 **Figure 4.** Rating of combinations with SFC and RUN.

271

272 **3.2.2 Sensitivities of physical processes and general behaviors of**

273 **parameterizations**

274 To further investigate the sensitivity of each process and the general performance

275 of the parameterizations, the Independent-sample T-test (2-tailed) and Tukey's test were

276 conducted to test whether the difference between parameterizations within a physical

277 process is significant (Fig. 5). In a given sub-process, any two schemes labelled with

278 different letters behave significantly different, and this sub-process therefore can be

279 identified as sensitive. Otherwise, the sub-process is considered insensitive. Moreover,

280 schemes with the letters late in the alphabet have smaller mean RMSEs and outperform

281   the ones with the letters forward in the alphabet. Using the three schemes in vegetation

282   model process (hereafter VEG(1), VEG(3) and VEG(4)) in Fig. 5 as an example. At the

283   depth of 5cm and 300cm, VEG(1) was labeled with letter "A", while VEG(3) and VEG

284   (4) was labeled with letter "B". For the depth of 25cm, 70cm, 140cm and 220cm,

285   VEG(1), VEG(3) and VEG(4) were labeled with the letter "A", "C" and "B",

286   respectively. As described above, the VEG process was sensitive for ST simulation.

287   Moreover, VEG(3) and VEG(4) had advantages in producing good simulations than

288   VEG(1) at 5cm and 300cm depths, and the performance decreased in the order of

289   VEG(3) > VEG(4) > VEG(1) at other layers. In terms of the whole soil column, VEG(3)

290   outperformed VEG(1) and VEG(4).

291   Consistent with the result in Fig. 3, all other physical processes showed

292   sensitivities in varying magnitudes except the BTR and CRS process. And the

293   performance difference between schemes of the RUN and SFC were obviously greater

294   than other processes. For the RUN process, the performance orders followed RUN(4) >

295   RUN(1) > RUN(2) > RUN(3) as a whole. Meanwhile, the difference between RUN(1)

296   and RUN(4) was indistinctive at the shallow layers (5 cm, 25 cm and 70 cm) and

297   significant but very small at the deep layers (140 cm, 220 cm and 300 cm). Moreover,

298   the performance orders were SFC(2) > SFC(1) for SFC process, FRZ(2) > FRZ(1) for

299   FRZ process, RAD(3) > RAD(1) > RAD(2) for RAD process, TBOT(1) > TBOT(2) for

300   TBOT process, and STC(2) > STC(1) for STC process. In particular, the FRZ process

301   showed sensitivity at the deep in spite of the shallow soil. Compared with INF(1), INF(2)

302   performed better at the shallow soils while did worse at the deep soils.
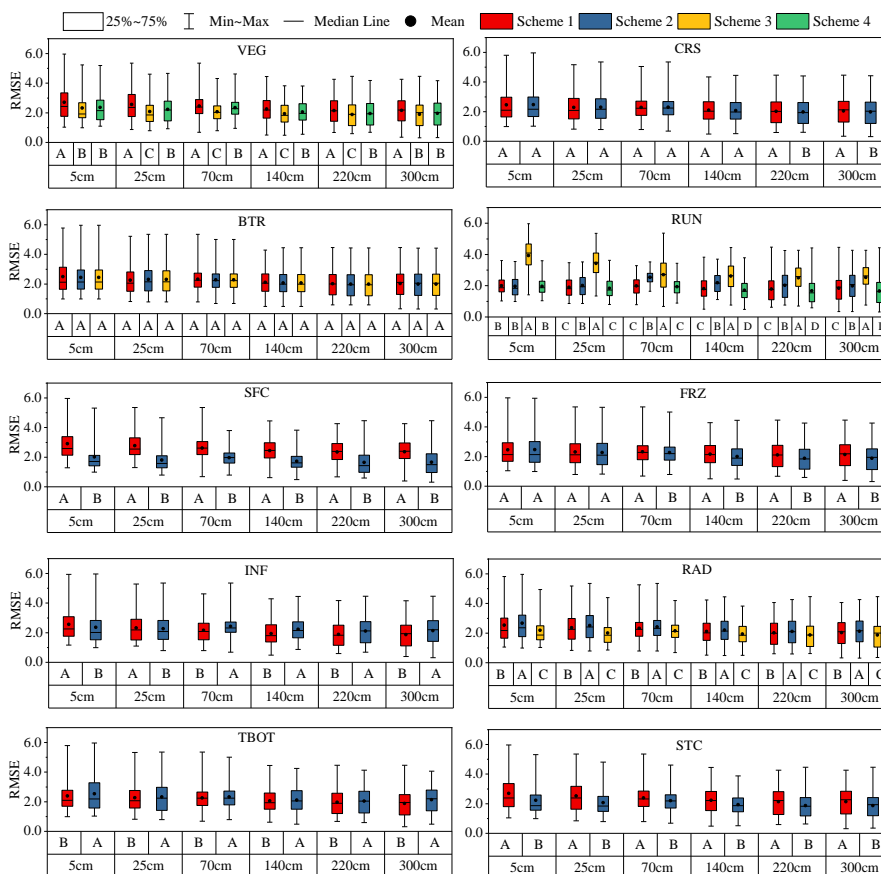
Figure 5. Distinction level for RMSE of ST at different layers in the ensemble simulations. Limits of the boxes represent upper and lower quartiles, whiskers extend to the maximum and minimum RMSE. The black stations in the box are the average values. The lines in the box indicate the median value.

3.3 The optimal combination

The CF was calculated to extract the optimal combination of parameterization schemes for ST simulation (Fig. 6). The CF between any two schemes from the same physical process was zero as expected. Consistent with Fig. 5, the CF of RUN(3) with other schemes was zero, implying that using RUN (3) provides an extreme less chance of producing favorable simulations than using RUN(1), RUN(2) or RUN(4). A higher

314   CF signify greater probability of producing advantageous simulations. For instance, the

315   CF between SFC(2) and VEG(3) was 0.45, about two times than the CFs between

316   SFC(2) and VEG(1)/VEG(4). It indicates that 45% of the 346 best combinations

317   adopted SFC(2) and VEG(3) simultaneously, and the combination of SFC(2) and

318   VEG(3) tend to inducing better ST in comparison of the combination of SFC(2) and

319   VEG(1)/VEG(4).

320   SFC(2) is firstly determined as one of the schemes that make up the optimal

321   combination, because it was most widely linked to other parameterization schemes with

322   relatively large CFs. Other optimal schemes of each physical process can be determined

323   by choosing the one that has large CF with SFC(2). Obviously, VEG(3), RUN(4),

324   FRZ(2) and INF(1) outperform other schemes in the corresponding physical processes

325   and were selected for optimal combination. The schemes within CRS, BTR, RAD and

326   STC processes scored nearly identical CFs with SFC(2). Due to the insensitivity of CRS

327   and BTR, CRS(1) and BTR(1), which are the default schemes in Noah-MP, were

328   determined as the member schemes of the optimal combination. Combining the selected

329   schemes above with different schemes of RAD and STC processes, there are 6

330   candidate combinations, among which the one with smallest colRMSE is selected as

331   the optimal combination. Ultimately, the determined schemes for optimal combination

332   is VEG(3), CRS(1), BTR(1), RUN(4), SFC(2), FRZ(2), INF(1), RAD(2), TBOT(2) and

333   STC(1) (Table 1).

334   The simulated results of the optimal scheme combination well captured the

335   variation of ST (Fig. 2). Despite the overestimation of ST at the shallow soil layers from

336   April to July, the optimal combination well produced the ST during the cold season and

337   of the deep layers (Fig. 2).

338

Geoscientific
Model Development
Discussions
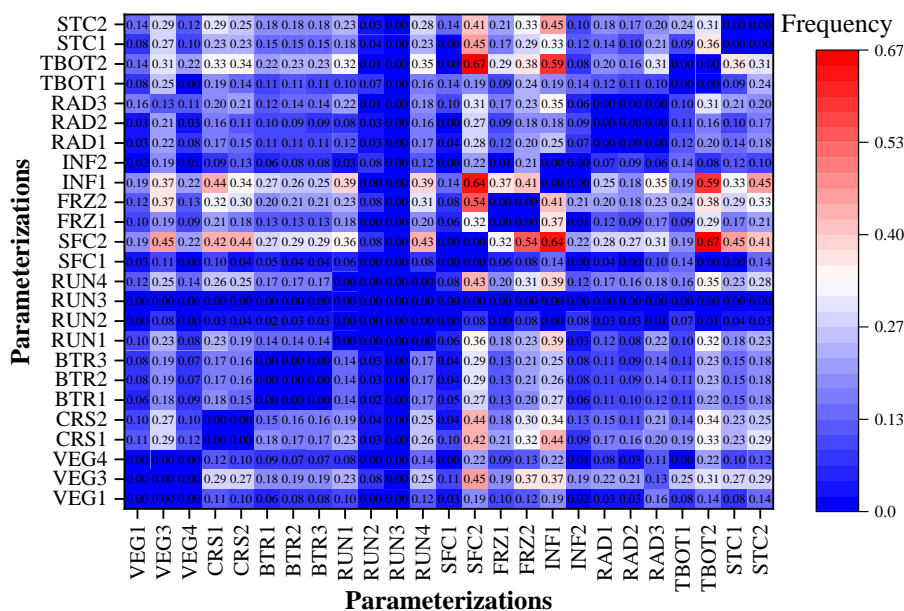
Figure 6. Connection frequency of parameterization schemes.

4 Discussion

4.1 Possible reasons for the cold bias of soil temperature

The cold bias of soil temperature on the QTP are widely reported in many of the state-of-the-art LSMs (Yang et al., 2009;Chen et al., 2019). One of the main reason can be the inability of representing the diurnal variation of roughness length for heat (Z_{0h}) on the QTP (Yang et al., 2008; Chen et al., 2010), which is of great importance for a reliable calculation of the sensible and latent heat, and thus for the soil surface/profile temperature calculation (Zeng et al., 2012; Zheng et al., 2012). Noah-MP parameterize Z_{0h} in the two schemes of SFC process (Table 1). In the M-O scheme, Z_{0h} is taken as the same with the roughness length for momentum (Z_{0m}, Niu et al., 2011). The Chen97 scheme adopts the Zilitinkevitch approach (Zilitinkevich, 1995). However, both of them couldn't produce the diurnal variation of $Z_{0,h}$ (Chen et al., 2010).

Another possible reason is the poor representation of the thermal conductivity (λ) of frozen soil. Considering that the λ of ice is nearly four times higher than liquid

17

Geoscientific
Model Development
Discussions

355 water, λ of frozen soil is generally expected to be greater than that of unfrozen soil.

356 Many parameterization schemes of λ, including the Johansen scheme in Noah-MP,

357 follow this pattern (Du et al., 2020). However, contrary phenomenon is widely reported

358 over the QTP (Pan et al., 2016; Hu et al., 2017; Yi et al., 2018; Li et al., 2019), including

359 the TGL site (Li et al., 2019). As a result, a majority of the state-of-the-art LSMs have

360 tended to overestimate the soil thermal conductivity of the QTP (Luo et al., 2009; Chen

361 et al., 2012; Du et al., 2020), which exactly explains the underestimation of soil

362 temperature during cold season and, at times, an overestimation during the warm season

363 (Luo et al., 2009).

364 **4.2 Discussions on the sensitivity of physical processes**

365 **4.2.1 Vegetation model (VEG) and canopy gap for radiation transfer (RAD)**

366 As list in Table 1, VEG process includes three options to calculate the variation of

367 vegetation fraction (FVEG) in this study. VEG(3) calculates the daily FVEG based on

368 the interpolated LAI, while VEG(1) and VEG(4) uses the prescribed monthly and

369 maximum LAI, respectively. Obviously, VEG(3) produces more realistic FVEG over

370 the year, followed by VEG(1) and VEG(4). VEG(4) grossly overestimates the FVEG,

371 especially that during the cold season. Consequently, VEG(3) outperformed VEG(1)

372 and VEG(4). However, VEG(4) is widely used in many studies (Gao et al., 2015; Chen

373 et al., 2016; Li et al., 2018) despite overestimating the FVEG. In this study, VEG(4)

374 performed better than VEG(1).

375 RAD treats the radiation transfer process within the vegetation, and adopts three

376 methods to calculate the canopy gap. RAD(1) defines canopy gap as a function of the

377 3D vegetation structure and the solar zenith angle, RAD(2) employs no gap within

378 canopy, and RAD(3) treat the canopy gap from unity minus the FVEG (Niu and Yang,

379 2004). The RAD(3) scheme penetrates the most solar radiation to the ground, followed

380 by the RAD(1) and RAD(2) schemes. As an alpine grassland, there is a relative low

381 LAI at TGL site, and thus a quite high canopy gap. So, schemes with a larger canopy

382 gap could realistically reflect the environment. Consequently, the performance

383   decreased in the order of RAD(3) > RAD(1) > RAD(2) for ST simulation.

4.2.2 Canopy stomatal resistance (CRS) and soil moisture factor for stomatal

resistance (BTR)

386   The biophysical process BTR and CRS directly affect the canopy stomatal

resistance and thus the plant transpiration (Niu et al., 2011). The transpiration of plants

could impact the ST through its cooling effect (Shen et al., 2015) and the water balance

of root zone (Chang et al., 2020). However, the annual transpiration of alpine steppe is

weak due to the shallow effective root zone and lower stomatal control in this dry

environment (Ma et al., 2015). As a result, the BTR process was insensitive at all layers.

CRS(1) and CRS(2) had no significant difference at most layers except the last two

layers. However, the performance difference between CRS(1) and CRS(2) at the last

two layers is very small (Fig. 3 and 5).

4.2.3 Runoff and groundwater (RUN)

396   For the RUN process, RUN(3) had the worst performance for simulating soil

moisture (Fig. S1) and thus for ST (Fig. 5) among the four schemes, likely due to its

free drainage assumption for subsurface runoff (Schaake et al., 1996), which is partly

consistent with the study of Zhang et al. (2016) that RUN(3) is the worst-performing

scheme for sensible and latent heat simulation in most cases compared with RUN(1)

and RUN(2). RUN(4) also adopts the free drainage concept. However, RUN(4)

outperformed RUN(3). It can be explained by the fourth power function of wetness at

the top 2-m soil in RUN(4), in which the partition of surface runoff and infiltration is

regulated by soil moisture (Yang and Dickinson, 1996). RUN(4) was on a par with

RUN(1) in the simulation of unfrozen water (Fig. S1). Consequently, there was no or

very small difference between RUN(4) and RUN(1) at shallow/deep soils (Fig. 5). For

the whole soil column, RUN(4) surpassed RUN(1) and RUN(2), both of which define

surface/subsurface runoff as functions of groundwater table depth (Niu et al., 2005; Niu

et al., 2007). This is in keeping with the study of Zheng et al. (2017) that soil water

storage-based   parameterizations   outperform   the   groundwater   table-based

411   parameterizations in simulating the total runoff in a seasonally frozen and high-altitude

412   Tibetan river, Besides, RUN(4) is designed based on the infiltration-excess runoff

413   (Yang and Dickinson, 1996) in spite of the saturation-excess runoff in RUN(1) and

414   RUN(2) (Gan et al., 2019), which is more common in arid and semiarid areas like the

415   permafrost regions of QTP (Pilgrim et al., 1988).

4.2.4 Surface layer drag coefficient (SFC)

417   SFC defines the calculations of the surface exchange coefficient for heat and water

418   vapor (CH), which greatly impact the energy and water balance and thus the

419   temperature of land surface. SFC(1) adopts the Monin-Obukhov similarity theory

420   (MOST) with a general form, while the SFC(2) uses the improved MOST modified by

421   Chen et al. (1997). The most distinct difference between them is that SFC(1) considers

422   the zero-displacement height while SFC(2) parameterizes Z_{0h} and Z_{0m} using different

423   schemes. The difference between SFC(1) and SFC(2) has a great impact on the CH

424   value. Several studies have reported that SFC(2) has a better performance for the

425   simulation of sensible and latent heat on the QTP (Zhang et al., 2016; Gan et al., 2019).

426   The results of Tukey's test in this study showed remarkable distinctions between the

427   two schemes, where SFC(2) was dramatically superior to SFC(1) (Fig. 5). SFC(2)

428   produces lower CH than SFC(1) (Zhang et al., 2014), resulting in less efficient

429   ventilation and greater heating of the land surface (Yang et al., 2011b), and substantial

430   improvement of the cold bias of Noah-MP in this study (Fig. 4).

4.2.5 Super-cooled liquid water (FRZ) and frozen soil permeability (INF)

432   FRZ treats unfrozen water (super-cooled liquid water) in frozen soil using two

433   forms of freezing-point depression equation. FRZ(1) takes a general form (Niu and

434   Yang, 2006), while FRZ(2) exhibits a variant form that considers the increased surface

435   area of icy soil particles (Koren et al., 1999). FRZ(2) generally yields more liquid water

436   in comparison of FRZ(1). In this study, FRZ process did not show sensitivity at the

437   shallow soil layers (5cm and 25cm), but showed an increasing sensitivity at the deep

438   layers (Fig. 3), which can be related to the longer frozen duration of deep soil.

439   INF(1) uses soil moisture (Niu and Yang, 2006) while INF(2) employs only the

440 liquid water (Koren et al., 1999) to parameterize soil hydraulic properties. INF(2)

441 generally produces more impermeable frozen soil than INF(1), which is also found in

442 this study (Fig. S2). Due to the more realistic representation of unfrozen water during

443 the cold season (Fig. S2), INF(2) surpassed INF(1) in simulating ST at 5 cm and 25 cm

444 depth, while INF(1) outperformed INF(2) at 70 cm, 140 cm and 220 cm (Fig. 5). This

445 result also indicate that INF(1) and INF(2) could alleviate the overestimation and

446 underestimation of unfrozen water, respectively. INF(2) performed worse than INF(1)

447 at 300 cm depth (Fig. 5) in spite of the better agreement with unfrozen water (Fig. S2),

448 which may be related to the overestimation of soil moisture of INF(2) at the depth of

449 140 cm.

4.2.6 Lower boundary of soil temperature (TBOT) and snow/soil temperature time
450

451 **scheme (STC)**

452 TBOT process adopts two schemes to describe the soil temperature boundary

453 conditions. TBOT (1) assumes zero heat flux at the bottom of the model, while TBOT(2)

454 adopts the soil temperature at the 8 m depth (Yang et al., 2011a). In general, TBOT(1)

455 is expected to accumulate heat in the deep soil and produce higher ST than TBOT(2).

456 In this study, the two assumptions performed significantly different, especially at the

457 deep soil. Although TBOT(2) is more representative of the realistic condition, TBOT(1)

458 surpassed TBOT(2) in this study. It can be related to the overall underestimation of the

459 model, which can be alleviated by TBOT(1) because of heat accumulation (Fig. S3).

460 Two time discretization strategies are implemented in the STC process, where

461 STC(1) adopts the semi-implicit scheme while STC(2) uses the full implicit scheme, to

462 solve the thermal diffusion equation in first soil or snow layers (Yang et al., 2011a).

463 STC(1) and STC(2) are not strictly a physical processes but different upper boundary

464 conditions of soil column (You et al., 2019). The differences between STC(1) and

465 STC(2) were significant (Fig. 5). Snow processes are not involved in this study, the

466 impacts of the two options on ST is remarkable (Fig. 5), particularly in the shallow

467 layers (Fig. 3). In addition, STC(2) outperformed STC(1) in the ensemble simulation

468 experiments (Fig. 5), because the higher ST produced by STC(2) (Fig. S4) alleviated

469   the overall estimation of Noah-MP.

4.3 Perspectives

471   We identified the systematic cold bias of Noah-MP and discussed the possible

472   sources of error, and analyzed the characteristics and general behavior of each

473   parameterization scheme at a permafrost site on the QTP. This work would be

474   constructive to a better understanding of the land surface processes on the QTP and

475   further model improvements towards near-surface permafrost modeling using the

476   LSMs.

477   Although the optimal combination demonstrated in this study is only from the

478   selected site, our results provide a practical way to investigate the permafrost state on

479   the QTP. The optimal combination well simulated the ST, especially that of deep layers

480   (Fig. 2). The representation of deep ST is crucial for permafrost modeling, which

481   directly affects the permafrost features such as active layer thickness and temperature

482   at the top of the permafrost. Further investigation with a broad spectrum of climate and

483   environmental conditions is necessary to make a general conclusion.

5   Conclusions

485   In this study, an ensemble simulation of soil temperature using multi-

486   parameterizations was conducted using the Noah-MP model at the TGL site, aiming to

487   provide a reference for permafrost simulation using LSMs. The model was modified to

488   consider the vertical heterogeneity in the soil and the simulation depth was extended to

489   cover the whole active layer. The ensemble simulation consists of 6912

490   parameterization experiments, combining ten physical processes (VEG, CRS, BTR,

491   RUN, SFC, FRZ, INF, RAD, TBOT, and STC) each with multiple optional schemes.

492   On this basis, the general performance of Noah-MP was assessed by comparing

493   simulation results with in situ observations, and the sensitivity of soil temperature at

494   different depth of active layer to parameterization schemes was explored. Furthermore,

22

495 we proposed a new method to extract the optimal combination of schemes to simulate

496 soil temperature in the permafrost regions of the QTP. The main conclusions are as

497 follows:

498 (1) Noah-MP model has relatively large uncertainties in the cold season, particularly at

499 the deep layers. Moreover, the model tends to underestimate soil temperature,

500 especially during the cold season. This is largely due to the imperfect model

501 structure with regard to the roughness length for heat and soil thermal conductivity.

502 (2) Soil temperature is dominated by the surface layer drag coefficient (SFC) while

503 largely influenced by runoff and groundwater (RUN). SFC(2) and RUN(3) could

504 significantly alleviate and aggravate the cold bias of soil temperature, respectively.

505 Other physical processes have little impact on ST simulation, among which VEG,

506 RAD, and STC are more influential on shallow ST, while FRZ, INF and TBOT have

507 greater impacts on deep ST. In addition, CRS and BTR do not significantly affect

508 the simulation results.

509 (3) The best scheme combination for permafrost simulation are as follows: VEG (table

510 LAI, calculated vegetation fraction), CRS (Jarvis), BTR (Noah), RUN (BATS),

511 SFC (Chen97), RAD (zero canopy gap), FRZ (variant freezing-point depression),

512 INF (hydraulic parameters defined by soil moisture), TBOT (ST at 8 m), STC (semi-

513 implicit).

514

515 *Code availability.* The source code of offline 1D Noah-MP LSM v1.1 is available at

516 https://ral.ucar.edu/solutions/products/noah-multiparameterization-land-surface-

517 model-noah-mp-lsm (last access: 15 May 2020). The modified Noah-MP with the

518 consideration of vertical heterogeneity, extended soil depth, and pedotransfer functions

519 is available upon request to the corresponding author. The data processing code are

520 available at http://dx.doi.org/10.17632/gc7vfgkyng.1.

521

522 *Data availability.* The 1-hourly forcing data and daily soil temperature data at the TGL

523 site are available at http://dx.doi.org/10.17632/gc7vfgkyng.1. Soil texture data can be

524 obtained at https://doi.org/10.1016/j.catena.2017.04.011 (Hu et al., 2017). The AVHRR

525 LAI data can be downloaded from https://www.ncei.noaa.gov/data/ (Claverie et al.,

526 2016).

527

528 *Author contributions.* TW and XL conceived the idea and designed the model

529 experiments. XL performed the simulations, analyzed the output, and wrote the paper.

530 XW, XZ, GH, RL contributed to the conduction of the simulation and interpretation of

531 the results. YQ provided the observations of atmospheric forcing and soil temperature.

532 CY and JH helped in downloading and processing the AVHRR LAI data. JN and WM

533 provide guidelines for the visualization. Everyone revised and polished the paper.

534

535 *Competing interests.* The authors declare that they have no conflict of interest.

536

541 **References**

542 Benjamini, Y.: Simultaneous and selective inference: Current successes and future challenges,
543   Biometrical J., 52, 708-721, https://doi.org/10.1002/bimj.200900299, 2010.
544 Cao, B., Zhang, T., Wu, Q., Sheng, Y., Zhao, L., and Zou, D.: Brief communication: Evaluation and
545   inter-comparisons of Qinghai–Tibet Plateau permafrost maps based on a new inventory of field
546   evidence, The Cryosphere, 13, 511-519, https://doi.org/10.5194/tc-13-511-2019, 2019.
547 Chang, M., Liao, W., Wang, X., Zhang, Q., Chen, W., Wu, Z., and Hu, Z.: An optimal ensemble of
548   the Noah-MP land surface model for simulating surface heat fluxes over a typical subtropical
549   forest in South China, Agric. For. Meteor., 281, 107815,
550   https://doi.org/https://doi.org/10.1016/j.agrformet.2019.107815, 2020.
551 Che, T., Hao, X., Dai, L., Li, H., Huang, X., and Xiao, L.: Snow cover variation and its impacts over
552   the Qinghai-Tibet Plateau, Bull. Chin. Acad. Sci., 34, 1247-1253,
553   https://doi.org/10.16418/j.issn.1000-3045.2019.11.007, 2019.
554 Chen, F., Janjić, Z., and Mitchell, K.: Impact of atmospheric surface-layer parameterizations in the
555   new land-surface scheme of the NCEP Mesoscale Eta Model. Boundary-Layer Meteorol. 85, 391-
556   421, https://doi.org/10.1023/A:1000531001463, 1997.

557   Chen, L., Li, Y., Chen, F., Barr, A., Barlage, M., and Wan, B.: The incorporation of an organic soil
558   layer in the Noah-MP land surface model and its evaluation over a boreal aspen forest, Atmos.
559   Chem. Phys., 16, 8375-8387, https://doi.org/10.5194/acp-16-8375-2016, 2016.

560   Chen, R., Yang, M., Wang, X., and Wan, G.: Review on simulation of land-surface processes on the
561   Tibetan Plateau, Sci. Cold Arid Reg., 11, 93-115, https://doi.org/10.3724/SP.J.1226.2019.00093,
562   2019.

563   Chen, S., Li, X., Wu, T., Xue, K., Luo, D., Wang, X., Wu, Q., Kang, S., Zhou, H., and Wei, D.: Soil
564   thermal regime alteration under experimental warming in permafrost regions of the central
565   Tibetan Plateau, Geoderma, 372, 114397,
566   https://doi.org/https://doi.org/10.1016/j.geoderma.2020.114397, 2020.

567   Chen, Y., Yang, K., Zhou, D., Qin, J., and Guo, X.: Improving the Noah Land Surface Model in Arid
568   Regions with an Appropriate Parameterization of the Thermal Roughness Length, J.
569   Hydrometeor., 11, 995-1006, https://doi.org/10.1175/2010JHM1185.1, 2010.

570   Chen, Y., Yang, K., Tang, W., Qin, J., and Zhao, L.: Parameterizing soil organic carbon's impacts
571   on soil porosity and thermal parameters for Eastern Tibet grasslands, Sci. Chin. Earth Sci., 55,
572   1001-1011, https://doi.org/10.1007/s11430-012-4433-0, 2012.

573   Claverie, M., Matthews, J. L., Vermote, E. F., and Justice, C. O.: A 30+ Year AVHRR LAI and
574   FAPAR Climate Data Record: Algorithm Description and Validation, Remote Sens., 8, 263,
575   https://doi.org/10.3390/rs8030263, 2016.

576   Cosby, B. J., Hornberger, G. M., Clapp, R. B., and Ginn, T. R.: A Statistical Exploration of the
577   Relationships of Soil Moisture Characteristics to the Physical Properties of Soils, Water Resour.
578   Res., 20, 682-690, https://doi.org/10.1029/WR020i006p00682, 1984.

579   Daniel, R., Nikolay, S., Bernd, E., Stephan, G., and Sergei, M.: Recent advances in permafrost
580   modelling, Permafr. Periglac. Process., 19, 137-156, https://doi.org/doi:10.1002/ppp.615, 2008.

581   Du, Y., Li, R., Zhao, L., Yang, C., Wu, T., Hu, G., Xiao, Y., Zhu, X., Yang, S., Ni, J., and Ma, J.:
582   Evaluation of 11 soil thermal conductivity schemes for the permafrost region of the central
583   Qinghai-Tibet Plateau, CATENA, 193, 104608,
584   https://doi.org/https://doi.org/10.1016/j.catena.2020.104608, 2020.

585   Fountain, A. G., Campbell, J. L., Schuur, E. A. G., Stammerjohn, S. E., Williams, M. W., and
586   Ducklow, H. W.: The Disappearing Cryosphere: Impacts and Ecosystem Responses to Rapid
587   Cryosphere Loss, BioScience, 62, 405-415, https://doi.org/10.1525/bio.2012.62.4.11, 2012.

588   Gan, Y. J., Liang, X. Z., Duan, Q. Y., Chen, F., Li, J. D., and Zhang, Y.: Assessment and Reduction
589   of the Physical Parameterization Uncertainty for Noah-MP Land Surface Model, Water Resour.
590   Res., 55, 5518-5538, https://doi.org/10.1029/2019wr024814, 2019.

591   Gao, Y., Kai, L., Fei, C., Jiang, Y., and Lu, C.: Assessing and improving Noah-MP land model
592   simulations for the central Tibetan Plateau, J. Geophys. Res.-Atmos., 120, 9258-9278, 2015.

593   Guo, D., and Wang, H.: Simulation of permafrost and seasonally frozen ground conditions on the
594   Tibetan Plateau, 1981-2010, J. Geophys. Res.-Atmos., 118, 5216-5230,
595   https://doi.org/10.1002/jgrd.50457, 2013.

596   Hillel, D.: Applications of Soil Physics, Academic Press, 400 pp., 1980.

597   Hjort, J., Karjalainen, O., Aalto, J., Westermann, S., Romanovsky, V. E., Nelson, F. E., Etzelmüller,
598   B., and Luoto, M.: Degrading permafrost puts Arctic infrastructure at risk by mid-century, Nat.
599   Commun., 9, 5147, https://doi.org/10.1038/s41467-018-07557-4, 2018.

600   Hong, S., Yu, X., Park, S. K., Choi, Y. S., and Myoung, B.: Assessing optimal set of implemented

601   physical parameterization schemes in a multi-physics land surface model using genetic algorithm,
602   Geosci. Model Dev., 7, 2517-2529, https://doi.org/10.5194/gmd-7-2517-2014, 2014.
603   Hu, G., Zhao, L., Li, R., Wu, T., Wu, X., Pang, Q., Xiao, Y., Qiao, Y., and Shi, J.: Modeling
604   hydrothermal transfer processes in permafrost regions of Qinghai-Tibet Plateau in China, Chin.
605   Geograph. Sci., 25, 713-727, https://doi.org/10.1007/s11769-015-0733-6, 2015.
606   Hu, G., Zhao, L., Wu, X., Li, R., Wu, T., Xie, C., Pang, Q., and Zou, D.: Comparison of the thermal
607   conductivity parameterizations for a freeze-thaw algorithm with a multi-layered soil in permafrost
608   regions, Catena, 156, 244-251, https://doi.org/10.1016/j.catena.2017.04.011, 2017.
609   Jin, H., Sun, L., Wang, S., He, R., Lu, L., and Yu, S.: Dual influences of local environmentalVariables
610   on ground temperatures on the interior-eastern Qinghai-Tibet Plateau (I): vegetation and snow
611   cover. J. Glaciol. Geocryol. 30, 535–545, 2008.
612   Koren, V., Schaake, J., Mitchell, K., Duan, Q. Y., Chen, F., and Baker, J. M.: A parameterization of
613   snowpack and frozen ground intended for NCEP weather and climate models, J. Geophys. Res.-
614   Atmos., 104, 19569-19585, https://doi.org/10.1029/1999JD900232, 1999.
615   Koven, C., Riley, W., and Stern, A.: Analysis of Permafrost Thermal Dynamics and Response to
616   Climate Change in the CMIP5 Earth System Models, J. Clim., 26, 1877-1900,
617   https://doi.org/10.1175/JCLI-D-12-00228.1, 2013.
618   Lawrence, D., Fisher, R., Koven, C., Oleson, K., Swenson, S., Vertenstein, M.: Technical description
619   of version 5.0 of the Community Land Model (CLM), Boulder, Colorado, 2018.
620   Li, J., Chen, F., Zhang, G., Barlage, M., Gan, Y., Xin, Y., and Wang, C.: Impacts of Land Cover and
621   Soil Texture Uncertainty on Land Model Simulations Over the Central Tibetan Plateau, J. Adv.
622   Model. Earth Sy., 10, 2121-2146, https://doi.org/10.1029/2018ms001377, 2018.
623   Li, R., Zhao, L., Wu, T., Wang, Q. X., Ding, Y., Yao, J., Wu, X., Hu, G., Xiao, Y., Du, Y., Zhu, X.,
624   Qin, Y., Shuhua, Y., Bai, R., Erji, D., Liu, G., Zou, D., Yongping, Q., and Shi, J.: Soil thermal
625   conductivity and its influencing factors at the Tanggula permafrost region on the Qinghai–Tibet
626   Plateau, Agric. For. Meteor., 264, 235-246, https://doi.org/10.1016/j.agrformet.2018.10.011,
627   2019.
628   Luo, S., Lyu, S., Zhang, Y., Hu, Z., Ma, Y. M., Li, S. S., and Shang, L.: Soil thermal conductivity
629   parameterization establishment and application in numerical model of central Tibetan Plateau,
630   Chin. J. Geophys., 52, 919-928, https://doi.org/10.3969/j.issn.0001-5733.2009.04.008, 2009.
631   Ma, N., Zhang, Y., Guo, Y., Gao, H., Zhang, H., and Wang, Y.: Environmental and biophysical
632   controls on the evapotranspiration over the highest alpine steppe, J. Hydrol., 529, 980-992,
633   https://doi.org/https://doi.org/10.1016/j.jhydrol.2015.09.013, 2015.
634   Maheu, A., Anctil, F., Gaborit, É., Fortin, V., Nadeau, D. F., and Therrien, R.: A field evaluation of
635   soil moisture modelling with the Soil, Vegetation, and Snow (SVS) land surface model using
636   evapotranspiration   observations   as   forcing   data,   J.   Hydrol.,   558,   532-545,
637   https://doi.org/https://doi.org/10.1016/j.jhydrol.2018.01.065, 2018.
638   Melton, J., Verseghy, D., Sospedra-Alfonso, R., and Gruber, S.: Improving permafrost physics in
639   the coupled Canadian Land Surface Scheme (v.3.6.2) and Canadian Terrestrial Ecosystem Model
640   (v.2.1) (CLASS-CTEM), Geosci. Model Dev., 12, 4443-4467, https://doi.org/10.5194/gmd-12-
641   4443-2019, 2019.
642   Nicolsky, D. J., Romanovsky, V. E., Alexeev, V. A., and Lawrence, D. M.: Improved modeling of
643   permafrost dynamics in a GCM land-surface scheme, Geophys. Res. Lett., 34, L08501,
644   https://doi.org/10.1029/2007gl029525, 2007.

Niu, G.-Y., and Yang, Z.-L.: Effects of vegetation canopy processes on snow surface energy and mass balances, J. Geophys. Res.-Atmos., 109, D23111, https://doi.org/10.1029/2004jd004884, 2004.

Niu, G.-Y., and Yang, Z.-L.: Effects of Frozen Soil on Snowmelt Runoff and Soil Water Storage at a Continental Scale, J. Hydrometeor., 7, 937-952, https://doi.org/10.1175/JHM538.1, 2006.

Niu, G.-Y., Yang, Z.-L., Dickinson, R. E., and Gulden, L. E.: A simple TOPMODEL-based runoff parameterization (SIMTOP) for use in global climate models, J. Geophys. Res.-Atmos., 110, D21106, https://doi.org/10.1029/2005jd006111, 2005.

Niu, G.-Y., Yang, Z.-L., Dickinson, R. E., Gulden, L. E., and Su, H.: Development of a simple groundwater model for use in climate models and evaluation with Gravity Recovery and Climate Experiment data, J. Geophys. Res.-Atmos., 112, D07103, https://doi.org/10.1029/2006jd007522, 2007.

Niu, G.-Y., Yang, Z.-L., Mitchell, K. E., Chen, F., Ek, M. B., Barlage, M., Kumar, A., Manning, K., Niyogi, D., and Rosero, E.: The community Noah land surface model with multiparameterization options (Noah-MP): 1. Model description and evaluation with local-scale measurements, J. Geophys. Res.-Atmos., 116, D12109, https://doi.org/10.1029/2010JD015139, 2011.

Pan, X., Li, Y., Yu, Q., Shi, X., Yang, D., and Roth, K.: Effects of stratified active layers on high-altitude permafrost warming: a case study on the Qinghai–Tibet Plateau, The Cryosphere, 10, 1591-1603, https://doi.org/10.5194/tc-10-1591-2016, 2016.

Pilgrim, D. H., Chapman, T. G., and Doran, D. G.: Problems of rainfall-runoff modelling in arid and semiarid regions, Hydrolog. Sci. J., 33, 379-400, https://doi.org/10.1080/02626668809491261, 1988.

Ran, Y., Xin, L., and Cheng, G.: Climate warming over the past half century has led to thermal degradation of permafrost on the Qinghai–Tibet Plateau, Cryosphere, 12, 595-608, https://doi.org/10.5194/tc-12-595-2018, 2018.

Schaake, J. C., Koren, V. I., Duan, Q. Y., Mitchell, K., and Chen, F.: Simple water balance model for estimating runoff at different spatial and temporal scales, J. Geophys. Res.-Atmos., 101, 7461-7475, https://doi.org/10.1029/95jd02892, 1996.

Shen, M., Piao, S., Jeong, S.-J., Zhou, L., Zeng, Z., Ciais, P., Chen, D., Huang, M., Jin, C.-S., Li, L. Z. X., Li, Y., Myneni, R. B., Yang, K., Zhang, G., Zhang, Y., and Yao, T.: Evaporative cooling over the Tibetan Plateau induced by vegetation growth, Proc. Natl. Acad. Sci. U. S. A., 112, 9299-9304, https://doi.org/10.1073/pnas.1504418112, 2015.

Wang, W., Yang, K., Zhao, L., Zheng, Z., Lu, H., Mamtimin, A., Ding, B., Li, X., Zhao, L., Li, H., Che, T., and Moore, J. C.: Characterizing Surface Albedo of Shallow Fresh Snow and Its Importance for Snow Ablation on the Interior of the Tibetan Plateau, J. Hydrometeor., 21, 815-827, https://doi.org/10.1175/JHM-D-19-0193.1, 2020.

Wei, Z., and Dong, W.: Assessment of Simulations of Snow Depth in the Qinghai-Tibetan Plateau Using CMIP5 Multi-Models, Arct. Antarct. Alp. Res., 47, 611-525, https://doi.org/10.1657/AAAR0014-050, 2015.

Westermann, S., Langer, M., Boike, J., Heikenfeld, M., Peter, M., Etzelmuller, B., and Krinner, G.: Simulating the thermal regime and thaw processes of ice-rich permafrost ground with the land-surface model CryoGrid 3, Geosci. Model Dev., 9, 523-546, https://doi.org/10.5194/gmd-9-523-2016, 2016.

Wetzel, P., and Chang, J.-T.: Concerning the Relationship between Evapotranspiration and Soil

689   Moisture, J. Clim. Appl. Meteorol., 26, 18-27, https://doi.org/10.1175/1520-
690   0450(1987)026<0018:CTRBEA>2.0.CO;2, 1987.

691 Woo, M. K.: Permafrost Hydrology, Springer, Berlin, Heidelberg, 2012.

692 Wu, X. B., Nan, Z. T., Zhao, S. P., Zhao, L., and Cheng, G. D.: Spatial modeling of permafrost
693   distribution and properties on the Qinghai-Tibet Plateau, Permafr. Periglac. Process., 29, 86-99,
694   https://doi.org/10.1002/ppp.1971, 2018.

695 Yang, K., Koike, T., Ye, B., and Bastidas, L.: Inverse analysis of the role of soil vertical
696   heterogeneity in controlling surface soil state and energy partition, J. Geophys. Res.-Atmos., 110,
697   D08101, https://doi.org/10.1029/2004jd005500, 2005.

698 Yang, K., Koike, T., Ishikawa, H., Kim, J., Li, X., Liu, H., Shaomin, L., Ma, Y., and Wang, J.:
699   Turbulent Flux Transfer over Bare-Soil Surfaces: Characteristics and Parameterization, J. Appl.
700   Meteorol. Clim., 47, 276-290, https://doi.org/10.1175/2007JAMC1547.1, 2008.

701 Yang, K., Chen, Y. Y., and Qin, J.: Some practical notes on the land surface modeling in the Tibetan
702   Plateau, Hydrol. Earth Syst. Sci., 13, 687-701, https://doi.org/10.5194/hess-13-687-2009, 2009.

703 Yang, Z.-L., and Dickinson, R. E.: Description of the biosphere-atmosphere transfer scheme (BATS)
704   for the soil moisture workshop and evaluation of its performance, Global Planet. Change, 13,
705   117-134, https://doi.org/10.1016/0921-8181(95)00041-0, 1996.

706 Yang, Z.-L., Cai, X., Zhang, G., Tavakoly, A., Jin, Q., Meyer, L., and Guan, X.: The Community
707   Noah Land Surface Model with Multi-Parameterization Options (Noah-MP): Technical
708   Description, 2011a.

709 Yang, Z.-L., Niu, G.-Y., E. Mitchell, K., Chen, F., B. Ek, M., Barlage, M., Longuevergne, L.,
710   Manning, K., Niyogi, D., Tewari, M., and Xia, Y.: The community Noah land surface model with
711   multiparameterization options (Noah-MP): 2. Evaluation over global river basins. J. Geophys.
712   Res.-Atmos. 116, D12110, https://doi.org/10.1029/2010JD015140, 2011b.

713 Yao, J., Zhao, L., Gu, L., Qiao, Y., and Jiao, K.: The surface energy budget in the permafrost region
714   of the Tibetan Plateau, Atmos. Res., 102, 394-407,
715   https://doi.org/https://doi.org/10.1016/j.atmosres.2011.09.001, 2011.

716 Yi, S., Zhou, Z., Ren, S., Ming, X., Yu, Q., Shengyun, C., and Baisheng, Y.: Effects of permafrost
717   degradation on alpine grassland in a semi-arid basin on the Qinghai–Tibetan Plateau, Environ.
718   Res. Lett., 6, 045403, https://doi.org/10.1088/1748-9326/6/4/045403, 2011.

719 Yi, S., He, Y., Guo, X., Chen, J., Wu, Q., Qin, Y., and Ding, Y.: The physical properties of coarse-
720   fragment soils and their effects on permafrost dynamics: a case study on the central Qinghai–
721   Tibetan Plateau, The Cryosphere, 12, 3067-3083, https://doi.org/10.5194/tc-12-3067-2018, 2018.

722 You, Y. H., Huang, C. L., Yang, Z. L., Zhang, Y., Bai, Y. L., and Gu, J.: Assessing Noah-MP
723   Parameterization Sensitivity and Uncertainty Interval Across Snow Climates, J. Geophys. Res.-
724   Atmos., 125, e2019JD030417, https://doi.org/10.1029/2019jd030417, 2020.

725 Zeng, X., Wang, Z., and Wang, A.: Surface Skin Temperature and the Interplay between Sensible
726   and Ground Heat Fluxes over Arid Regions, J. Hydrometeor., 13, 1359-1370,
727   https://doi.org/10.1175/JHM-D-11-0117.1, 2012.

728 Zhang, G., Chen, F., and Gan, Y.: Assessing uncertainties in the Noah-MP ensemble simulations of
729   a cropland site during the Tibet Joint International Cooperation program field campaign, J.
730   Geophys. Res.-Atmos., 121, 9576-9596, https://doi.org/10.1002/2016jd024928, 2016.

731 Zhang, T.: Influence of the seasonal snow cover on the ground thermal regime: An overview,
732   Reviews of Geophysics, 43, RG4002, https://doi.org/10.1029/2004RG000157, 2005.

733   Zhao, L., Hu, G., Zou, D., Wu, X., Ma, L., Sun, Z., Yuan, L., Zhou, H., and Liu, S.: Permafrost
734   changes and its effects on hydrological processes on Qinghai-Tibet Plateau, Bull. Chin. Acad.
735   Sci., 34, 1233-1246, https://doi.org/10.16418/j.issn.1000-3045.2019.11.006, 2019.

736   Zheng, D., Van Der Velde, R., Su, Z., Wen, J., and Wang, X.: Assessment of Noah land surface
737   model with various runoff parameterizations over a Tibetan river, J. Geophys. Res.-Atmos., 122,
738   1488-1504, https://doi.org/10.1002/2016jd025572, 2017.

739   Zheng, H., Yang, Z.-L., Lin, P., Wei, J., Wu, W.-Y., Li, L., Zhao, L., and Wang, S.: On the sensitivity
740   of the precipitation partitioning into evapotranspiration and runoff in land surface
741   parameterizations, Water Resour. Res., 55, 95-111, https://doi.org/10.1029/2017WR022236,
742   2019.

743   Zheng, W., Wei, H., Wang, Z., Zeng, X., Meng, J., Ek, M., Mitchell, K., and Derber, J.: Improvement
744   of daytime land surface skin temperature over arid regions in the NCEP GFS model and its impact
745   on satellite data assimilation, J. Geophys. Res.-Atmos., 117, D06117,
746   https://doi.org/10.1029/2011jd015901, 2012.

747   Zilitinkevich, S.: Non-local turbulent transport pollution dispersion aspects of coherent structure of
748   convective flows, Air Pollution III, Air pollution theory and simulation (H Power, N
749   Moussiopoulos, C A Brebbia, eds) Computational Mechanics Publ , Southampton, Boston, 1, 53-
750   60, 1995.

751   Zou, D., Zhao, L., Sheng, Y., Chen, J., Hu, G., Wu, T., Wu, J., Xie, C., Wu, X., Pang, Q., Wang, W.,
752   Du, E., Li, W., Liu, G., Li, J., Qin, Y., Qiao, Y., Wang, Z., Shi, J., and Cheng, G.: A new map of
753   permafrost distribution on the Tibetan Plateau, The Cryosphere, 11, 2527-2542,
754   https://doi.org/10.5194/tc-11-2527-2017, 2017.

755